

# Influence of Feedstock on the Microstructure of $\text{Sm}_2\text{Zr}_2\text{O}_7$ Thermal Barrier Coatings Deposited by Plasma Spraying

Wei Guo<sup>1,2</sup> · Zhuang Ma<sup>1,2</sup> · Ling Liu<sup>1,2</sup> · Yanbo Liu<sup>1,2</sup>

Submitted: 5 September 2018 / in revised form: 24 October 2018 / Published online: 27 November 2018  
© ASM International 2018

**Abstract** Four  $\text{Sm}_2\text{Zr}_2\text{O}_7$  (SZO) powders with different morphologies were deposited by atmospheric plasma spraying on superalloy substrates using the same spraying parameters. Both the particle size distribution and microstructure of the powders had an important effect on the coating microstructure. SZO thermal barrier coatings (TBCs) deposited using the powder with a narrow particle size distribution showed a better “molten state” and exhibited a higher average bonding strength compared with the SZO TBCs deposited using the powder with a wide particle size distribution. The dense microstructure of the calcined powder sintered at high temperature and of the powder spheroidized by plasma spraying gun (SF) improved the melting capacity of the powders, and the resulting coatings showed a compact microstructure with unique bimodal structures. Furthermore, the SF SZO TBCs presented an excellent “molten state” with a smooth surface and exhibited a high bonding strength of  $29.6 \pm 0.15$  MPa.

**Keywords** microstructures · plasma spraying · rare-earth zirconates · thermal barrier coatings

## Introduction

Plasma-sprayed thermal barrier coatings (TBCs) have found wide applications in protection of high-temperature metallic components such as turbine engines by decreasing the temperature seen by the substrate or increasing the thermal efficiency (Ref 1-4). However, their potential for application at even higher temperatures (i.e., above 1200 °C) is very limited due to the sintering and phase transformation of the conventional outer ceramic yttria-stabilized zirconia (YSZ) layer (Ref 5-9). The search for new materials with properties superior to those of conventional YSZ is intensifying.

Rare-earth zirconates were recently proposed as a series of promising materials (Ref 10-13).  $\text{Sm}_2\text{Zr}_2\text{O}_7$  (SZO) shows lower thermal conductivity (1.6 W/m-K) than that of 8YSZ (2.2 W/m-K) (Ref 14, 15). It is thermally stable up to 1900 °C and has attracted great attention. Previous investigations illustrated that plasma-sprayed (PS) SZO coatings exhibited moderate performance and were not appropriate for such applications. In fact, the microstructure and properties of plasma-sprayed coatings are significantly affected by the characteristics of the feedstock, such as its morphology, size distribution, and flowability, as well as the conditions of the spraying process (Ref 16). All of these factors have a strong influence on the heat and momentum transfer between the feedstock and plasma jet. Therefore, it is important to determine whether SZO coatings can exhibit excellent thermomechanical properties if the spray process and feedstock powders are improved. However, little information is

---

✉ Ling Liu  
richard@bit.edu.cn

Wei Guo  
weigu9417@gmail.com

Zhuang Ma  
hstrong929@bit.edu.cn

Yanbo Liu  
boobby@163.com

<sup>1</sup> School of Materials Science and Engineering, Beijing Institute of Technology, Beijing 100081, China

<sup>2</sup> National Key Laboratory of Science and Technology on Materials under Shock and Impact, Beijing 100081, China

currently available regarding the effect of the feedstock powder on the structure and properties of PS coatings. In the work presented herein, SZO feedstock powders with different size distributions and original grain sizes were prepared for deposition of TBCs using a PS system. The influence of the feedstock powder on the microstructure and bonding strength of the resulting SZO coatings was then investigated.

## Experimental Procedures

### Preparation of Feedstocks for Thermal Spraying

The agglomerated SZO feedstock used for PS was obtained by a chemical coprecipitation and spray drying granulation method, as described in Ref 17, 18. The suspension for spray-drying, composed of SZO powder, polyvinyl alcohol (PVA, 0.5 wt.%), and deionized water, was ball-milled for longer than 2 h. The solids content of the suspension was 50%. Subsequently, the suspension was sprayed into small droplets using a LGZ-8 spray dryer. The droplets quickly dried in the hot air, forming microspheres. The spray-dried powders showed a near-spherical morphology; the morphology and particle size distribution are presented in

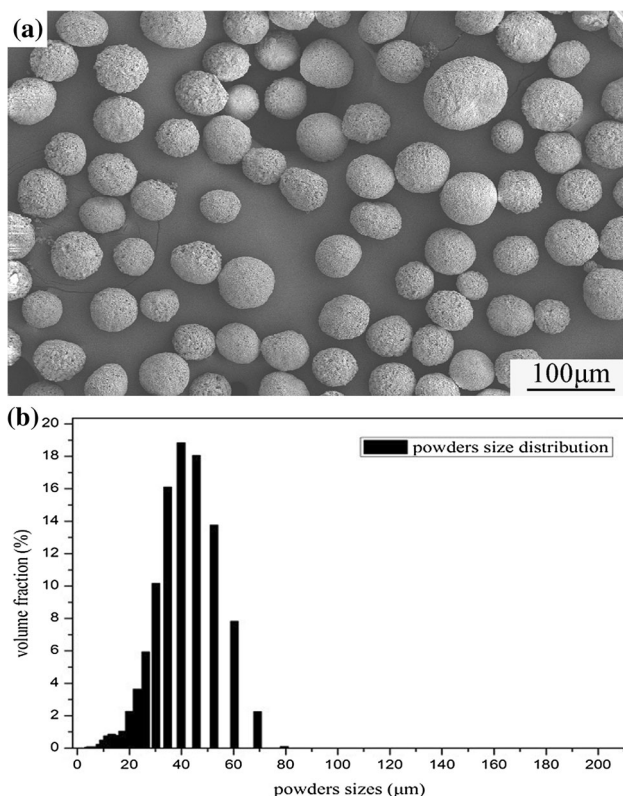


**Fig. 1** The morphology (a) and size distribution (b) of the spray-dried SZO powders

Fig. 1. The spray-dried powders were calcined at 1100 °C for 2 h. Two types of sprayable SZO feedstock powder with different size distributions were collected. The first feedstock exhibited a wide size distribution in the range of 20–80 μm, being denoted as “WF.” The second feedstock exhibited a narrow size distribution in the range of 20–50 μm, being denoted as “NF.” To increase their apparent density and flowability, the calcined SZO feedstock powders were sintered at high temperature of 1600 °C for 3 h (named “HF”) and spheroidized by using a plasma spray process (named “SF”), respectively. The size distribution of the HF and SF powders was 35–65 μm. The main parameters used for the plasma spheroidizing process are presented in Table 1. The powders were heated and melted by a plasma jet, then directly cooled and collected in deionized water for drying (Ref 19).

### Preparation of Coatings

All the coatings were fabricated by PS (SG100 spray gun, PRAXAIR-TAFA, USA). The primary gas and auxiliary gas used in PS were argon and helium, respectively. Before spraying, the surface of the IC10 nickel-based superalloy substrates was cleaned using acetone for degreasing. The substrates were then grit-blasted to achieve a rough surface to increase the bonding strength. Then, NiCoCrAlY (CO-210, Praxair, USA) as the bond coating (about 100 μm in thickness) and SZO as the top coating (about 200 μm in thickness) were deposited onto the superalloy substrates in turn to prepare the SZO TBCs. The plasma spraying parameters are listed in Table 2.

### Characterization

The microstructure of the feedstock powders and the surface and cross-section morphology of the SZO coatings were observed by scanning electron microscopy (SEM, S-4800, Tokyo, Japan). The porosity of the coatings was estimated by quantitative metallography (LECO IA32-VideoTest Master, Lakeview Ave, USA) (on at least 10

**Table 1** Parameters used in the plasma spheroidizing process

Parameter	Numerical value
Current, A	950
Voltage, V	75
Flow rate of auxiliary gas (SCFH)	50
Flow rate of primary gas (SCFH)	80
Feedstock supply rate, g/min	3.0
Spray distance, mm	120

SCFH standard cubic feet per hour

images for each type of pellet) in conjunction with image analysis. The bonding strength of the coatings was tested using an electronic universal tensile machine (model WDW-E100, Anduo Trade Co. Ltd., Nanjing, China). The coated stubs were adhered to coupling stubs using a cold-cured adhesive glue (3M, SW2214, Japan) to investigate the mechanical bonding strength.

## Results and Discussion

### Microstructure of Feedstock Powders

The morphology and microstructure of the feedstock powders prepared using the different thermal treatment processes are shown in Fig. 2. The feedstock powders

**Table 2** Parameters used in the atmospheric plasma spraying

Parameter	NiCoCrAlY	SZO
Current, A	700	850
Voltage, V	65	75
Flow rate of auxiliary gas (SCFH)	120	80
Flow rate of primary gas (SCFH)	10	50
Feedstock supply rate, g/min	2	2
Spray distance, mm	75	75
Spray inclusion, °	90	90

calcined at 1100 °C for 2 h displayed good sphericity. The spheres comprised submicron (0.1–0.6 μm) grains and were loose and porous (Fig. 2a). From Fig. 2(b), it can be seen that the powders sintered at 1600 °C for 3 h were relatively compact, but some pores were still present among the grains. Meanwhile, the sphericity of the HF powders became poor due to their irregular shrinkage during the sintering process. The internal grains were obviously sintered and grew to micron scale (about 1–2 μm).

Figure 2(c) and (d) show the surface and cross-section microstructure of SF. Near-perfect spherical powder was obtained, exhibiting three forms: hollow powder, solid powder with loose particles inside, and solid powder with dense particles inside. This result indicates that small (less than 40 μm) and hollow agglomerated powders could be fully melted in the plasma jet. The larger solid powders showed a sintered shell with thickness of 3–5 μm, retaining some unmelted particles in the center with a grain size of 0.2–0.4 μm. During plasma spraying, the momentum and energy transfer processes between the plasma and powder are crucial to the melting state of the in-flight particles. When the powder is injected into the plasma jet, the temperature at its surface can increase rapidly. However, the melting condition for the powder depends on its size and thermal conductivity. For larger SZO powder with low thermal conductivity, the temperature is high at the surface but low at the center. Therefore, the particles at the surface

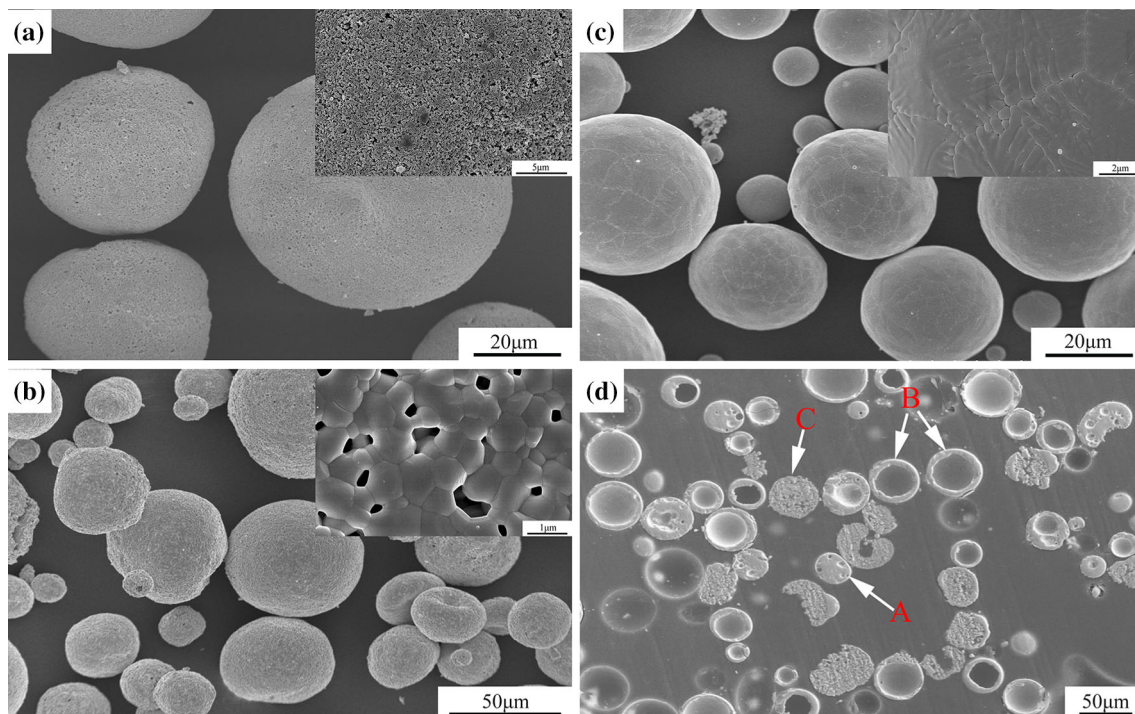


**Fig. 2** The morphology and microstructure of the feedstock powders prepared using different thermal treatment processes: (a) calcination at 1100 °C for 2 h, (b) HF, and (c, d) surface and cross-sectional microstructure of SF



are melted more easily, while some unmelted particles remain in the center.

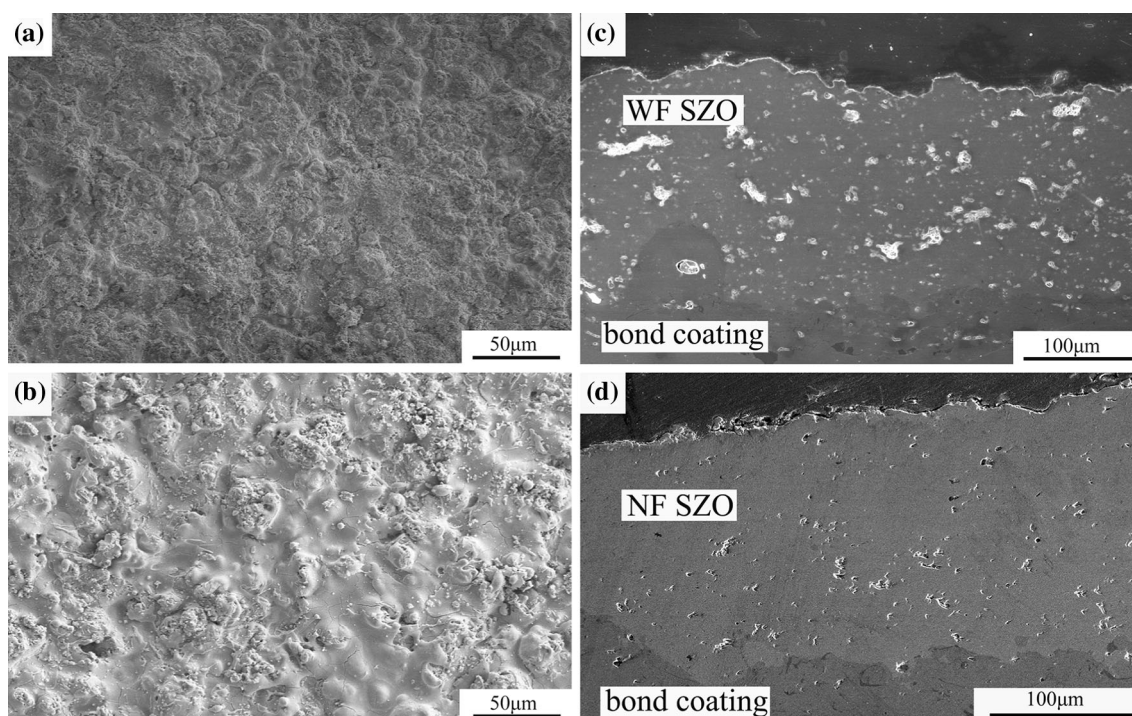
### Microstructure of Coatings Deposited Using Feedstocks with Different Size Distributions

Figure 3 shows the SEM microstructure of the SZO coatings deposited using the WF and NF powders. The surface of both as-sprayed coatings was uneven without nonmolten particles, as shown in Fig. 3(a) and (b), but there were more fully molten areas on the surface of the NF SZO coating, implying a better molten state. The cross-sectional morphology of the WF SZO (Fig. 3c) and NF SZO (Fig. 3d) as-sprayed coatings showed that both presented a certain quantity of pores and microcracks, because of the deposition of nonmolten particles or the inhomogeneous deposition of the molten drops during the spreading process. The porosity of the WF SZO coatings as determined by image analysis was almost at the level of  $\sim 11.4\%$ , slightly higher than the porosity of the NF SZO coating ( $\sim 9.3\%$ ). It is easy to see that the pores in the NF SZO coatings were relatively fine compared with those in the WF SZO coatings.

It can be seen that typical lamellar structures with columnar grains formed by directional solidification at this cooling rate (Ref 20, 21). However, the fracture cross-sectional morphology of the WF and NF SZO coatings

showed differences. A certain quantity of pores and microcracks could be observed in the fracture cross-sectional SEM micrograph of the WF SZO coating (Fig. 4a). Figure 4(b) shows a cross-sectional SEM micrograph from a nonmolten region near the pores (similar to that indicated by the red box in Fig. 4a), showing loose equiaxed grains between columnar grains. These loose structure and defects may weaken the bonding strength. The average bonding strength of the coatings is presented in Table 3. The average bonding strength of the WF SZO TBCs was  $15.1 \pm 0.08$  MPa. Compared with the WF SZO coating, as can be seen in Fig. 4(c), the fracture cross-section morphology of the NF SZO coating was dense. In addition, the proportion of columnar grain structures increased apparently and the pores were finer than the coating mentioned above, having a positive impact on the bonding strength. The bonding strength results for the SZO TBCs deposited using NF powder showed an average value of  $28.6 \pm 0.14$  MPa, about two times higher than that of the WF SZO TBCs. Figure 4(d) shows a cross-sectional SEM micrograph of a half-molten region (similar to that indicated by the white box in Fig. 4a), showing a dense binding state of columnar and equiaxed grains.

In general, the size of the feedstock powder is a critical parameter for the formation of the microstructure of the coating when using given spraying parameters. When heated by the plasma flame, the large bulk volume of the



**Fig. 3** SEM micrographs of (a) the surface morphology of the WF SZO TBCs, (b) the surface morphology of the NF SZO TBCs, (c) the cross-section morphology of the WF SZO TBCs, (d) the cross-section morphology of the NF SZO TBCs

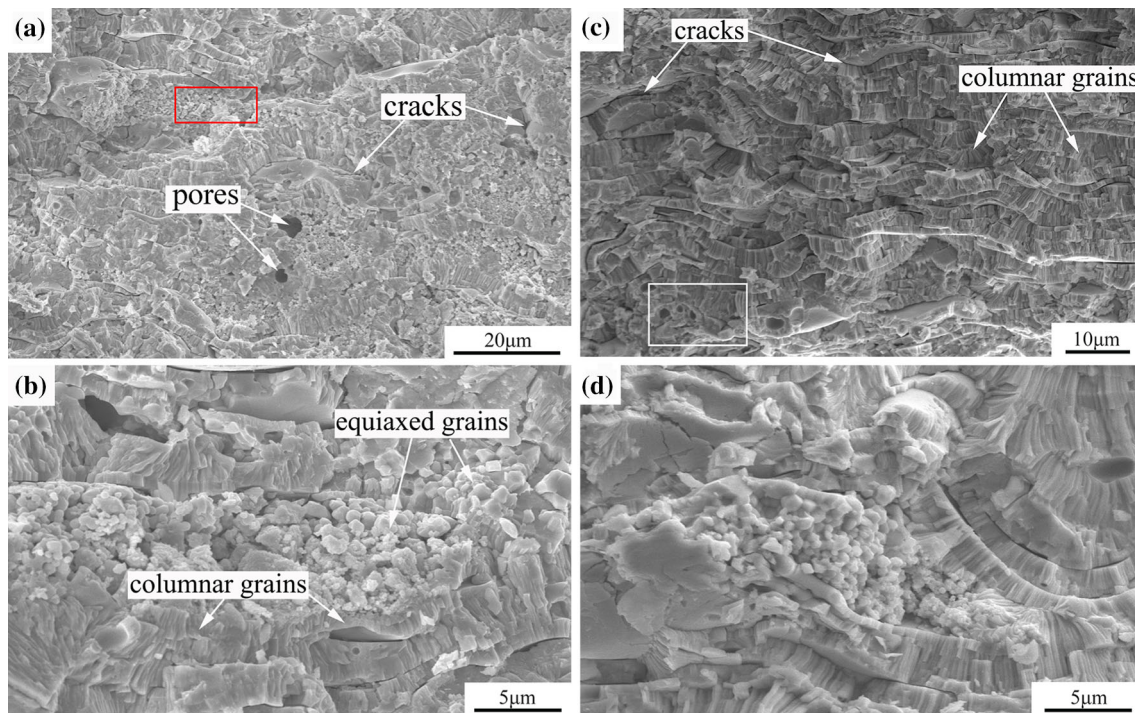


**Fig. 4** Fractured microstructure of SZO coatings: (a, b) WF SZO coating at low and high magnification, respectively; (c, d) NF SZO coatings at low and high magnification, respectively

**Table 3** Average bonding strength of coatings

Sample	Average bonding strength, MPa
WF SZO TBCs	$15.1 \pm 0.08$
NF SZO TBCs	$28.6 \pm 0.14$
HF SZO TBCs	$31.5 \pm 0.16$
SF SZO TBCs	$29.6 \pm 0.15$

coarse (50–80  $\mu\text{m}$ )  $\text{Sm}_2\text{Zr}_2\text{O}_7$  powder with low thermal conductivity hinders heat transport from the surface to the core of the powder. As a consequence, it is difficult to attain a sufficient molten state before deposition of the coating for such coarse powders, and nonmolten particles will be embedded in the splat, which accounts for the formation of giant pores and cracks (Fig. 4a). In contrast to coarse powders (50–80  $\mu\text{m}$ ), the small bulk volume of fine (20–50  $\mu\text{m}$ ) powders is beneficial to heat transport. Thus, during the spraying process, such fine (20–50  $\mu\text{m}$ ) powders can fully melt and turn into molten drops, enabling uniform spreading on the substrate to form adherent lamellar structures (Fig. 4c). Hence, it is interesting to note that a narrow size distribution of the SZO feedstock powder is favorable for plasma spraying.

### Microstructure of Coatings Deposited Using Feedstocks with Different Microstructural Characteristics

Figure 5(a) shows the surface morphology of the SZO TBCs deposited using HF. An inhomogeneous distribution of partially molten particles can be observed on the surface of the HF SZO coating. In striking contrast to the SZO TBCs mentioned above, as shown in Fig. 5(b), the surface of the SF SZO coating showed large, continuous, dense and smooth areas, whereas nonmolten particles could hardly be found. It can be seen that the fully melted powder spread out on the surface of the coating. Figure 5(c) shows the cross-sectional morphology of the SF SZO coating, revealing strong adhesion with the bond coating. In addition, the porosity of the SF SZO coating was the lowest among these coatings, estimated at  $\sim 6.7\%$ . When heated by the plasma jet, its continuous and compact structure enhances the thermal conductivity of the SZO SF powder, and the temperature of the powder center will increase rapidly. Meanwhile, the excellent flowability boosts the dispersibility of the SZO SF powder in the plasma jet, giving all the particles the opportunity to melt sufficiently and spread homogeneously on the substrate.

Figure 6(a) shows a fractured cross-sectional SEM micrograph of the HF SZO TBCs. The microstructure is more compact with fewer microcracks and pores, appearing only between the two lamellar structures with columnar



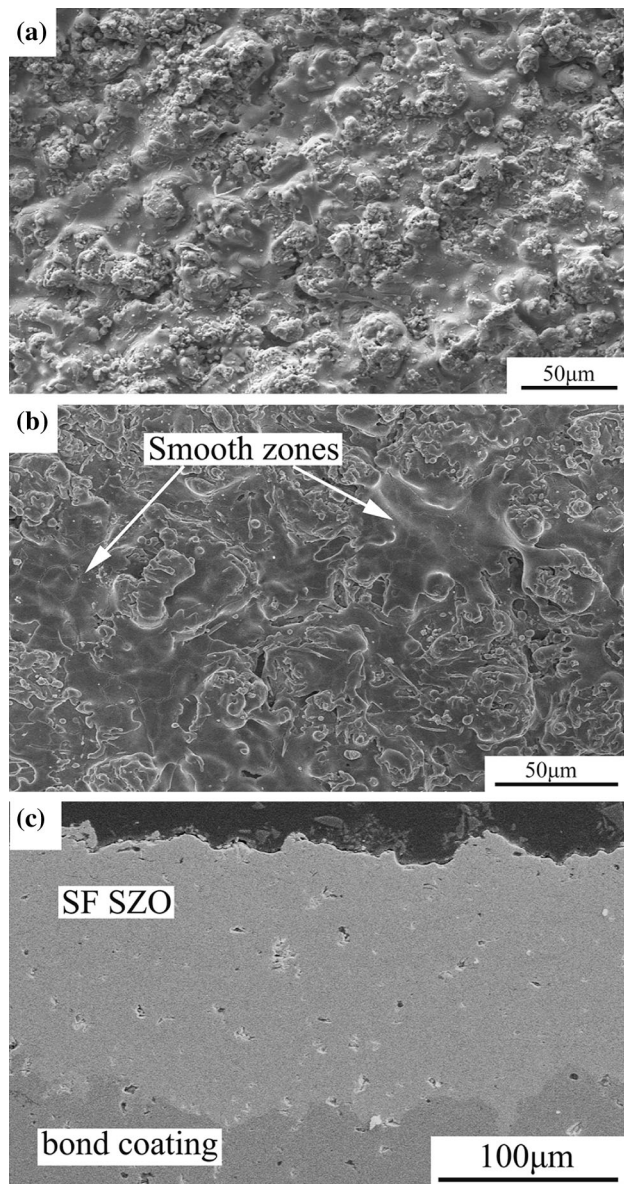


**Fig. 5** Morphology of SZO coatings deposited using HF and SF powders: (a) surface of HF SZO coating; (b) surface of SF SZO coating; (c) cross-section of SF SZO coating

grains. It is interesting to note that some submicron globular grains can be observed in the magnified region near the pores, shown in Fig. 6(b). It appears that the submicron globular grains result from partial melting and recrystallization of the sufficiently melted HF SZO particles in the process of heating and cooling, since the HF powders are micron-sized grains (Fig. 2b). Figure 6(c) shows the fractured cross-section morphology of the SF SZO coating, revealing an evident special multilayer lamellar structure. One type of region, e.g., Z1 in Fig. 6(c), shows a very compact columnar crystal area with no gaps or defects. Also, there are some pores and cracks between the inter-layers, which is inevitable in plasma-sprayed coatings (Ref

22). Figure 6(d) shows an equiaxed grain region (similar to region Z2 in Fig. 6c) at higher magnification. Compared with the loose equiaxed grains of the WF SZO coating (Fig. 4b), the equiaxed-shaped nanograins of the SF SZO coating are sintered and tightly adhered to each other.

The results presented here clearly show that the microstructure of the powder plays an important role in the microstructure of the resulting coating. The dense microstructure of the powders sintered at 1600 °C for 3 h accelerated heat transport and improves the molten state of the HF powders. This is why the SZO HF powder can be sufficiently melted and form the submicron globular recrystallized microstructure. Moreover, the sufficient molten state can enhance the bonding of layers and decrease the quantity of cracks and porosity, which is favorable to increase the bonding strength of the coating.

In contrast to the other SZO TBCs discussed above, the fracture cross-section of the SF coating showed a special molten area composed of bimodal structures and an extraordinary molten state. The three morphologies of the spheroidized feedstock (shown in Fig. 2d) discussed above play a key role in the formation of the special microstructure. When heated by the plasma jet, because the structure of the solid powder with dense particles (powder A in Fig. 2d) favors its melting, the melted drops impact on the substrate and form the dense columnar grain structure. While the hollow powder (powder B in Fig. 2d) can be fully melted during the heat treatment, the empty center of the powder is inclined to form cracks and pores. An important point to note is that some powder with core–shell structure, consisting of solid powder with loose nanosize particles inside, is present in the spheroidized feedstock (powder C in Fig. 2d). During the spraying process, although the temperature at the surface is high, the porous microstructure blocks heat transport, resulting in a low internal temperature. Therefore, the internal nanosize particles undergo a certain degree of sintering and the nanoequiaxed grains are preserved, which is beneficial to improve the thermal insulation ability of the coating (Ref 23) and reduce its in-plane Young’s modulus significantly (Ref 24–27).

The bonding strength results for the SZO TBCs deposited using SF showed an average value of  $29.6 \pm 0.15$  MPa, roughly equivalent to that of SZO TBCs (about  $31.5 \pm 0.16$  MPa) deposited using HF with the same powder size. The powder grains grew to micron size when calcined at high temperature. The resulting SZO coating will therefore demonstrate a compact state, which will favor increased bonding strength of the coating. Although the unmelted phases can decrease the thermal conductivity of the coating, the loose structure and weak bonding strength of the unmelted phases have adverse effects on the mechanical properties of the coating.

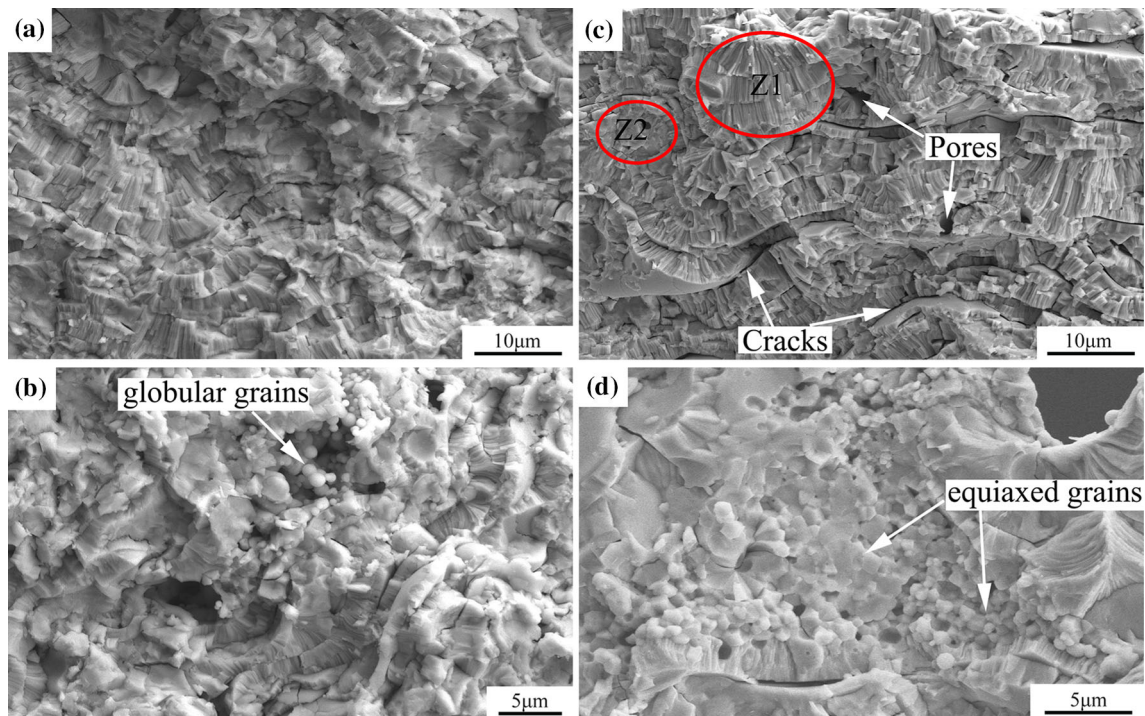


**Fig. 6** Fracture microstructure of the SZO coatings: (a) and (b) HF SZO coatings at low and high magnification, respectively; (c) and (d) SF SZO coatings at low and high magnification, respectively

Therefore, it is more desirable to obtain sintered equiaxed grains in the coating to improve the bonding strength. Besides, the equiaxed grains can also contribute to the decrease of thermal conductivity. When the SZO coatings were deposited using spheroidized feedstock, according to the fracture surface of the coating, the molten phase was composed of bimodal structures, which can be beneficial to improve the toughness of the coating and enhance its mechanical properties.

## Conclusions

$\text{Sm}_2\text{Zr}_2\text{O}_7$  feedstock powders with four different morphologies (WF, NF, HF, and SF) were prepared by thermal treatment and spheroidized by plasma spraying gun, then deposited on superalloy substrates by atmospheric plasma spraying. The WF SZO TBCs showed a loose microstructure with a certain quantity of pores and cracks, due to the unfavorable molten state of the wide range of large-size powders. The narrow range of small-size powders showed a better molten state, and the bonding strength of the corresponding coating exhibited an average value of  $28.6 \pm 0.14$  MPa, nearly two times higher than that of WF SZO TBCs ( $15.1 \pm 0.08$  MPa). The microstructure of the coatings deposited using HF showed a compact state, because the dense microstructure of the feedstock powders benefits the melting of the powders. The SZO TBCs

deposited using SF exhibited an extraordinary molten state and unique bimodal structure, which may be advantageous for the thermal insulation performance. This is attributed to the special core–shell microstructure of the SF. These results indicate that a narrow range and reasonable morphology of the feedstock powder are beneficial to improve the bonding strength of TBCs.

**Acknowledgments** This work was financially supported by the National Natural Science Foundation of China (No. 51772027).

## References

1. N.P. Padture, M. Gell, and E.H. Jordan, Thermal Barrier Coatings for Gasturbine Engine Applications, *Science*, 2002, **296**, p 279–284
2. E. Bakan and R. Vaßen, Ceramic Top Coats of Plasma-Sprayed Thermal Barrier Coatings: Materials, Processes, and Properties, *J. Therm. Spray Technol.*, 2017, **26**(6), p 992–1010
3. C.U. Hardwicke and Y.C. Lau, Advances in Thermal Spray Coatings for Gas Turbines and Energy Generation: A Review, *J. Therm. Spray Technol.*, 2013, **22**, p 564–576
4. W.W. Zhang, G.R. Li, Q. Zhang, and G.J. Yang, Comprehensive Damage Evaluation of Localized Spallation of Thermal Barrier Coatings, *J. Adv. Ceram.*, 2017, **6**(3), p 230–239
5. R. Vassen, X.Q. Cao, F. Tietz, D. Basu, and D. Stöver, Zirconates as New Material for Thermal Barrier Coatings, *J. Am. Ceram. Soc.*, 2000, **83**(8), p 2023–2028
6. H. Lehmann, D. Pitzer, G. Pracht, R. Vassen, and D. Stöver, Thermal Conductivity and Thermal Expansion Coefficients of the

- Lanthanum Rare-Earth-Element Zirconate System, *J. Am. Ceram. Soc.*, 2003, **86**(8), p 1338-1344
7. N. Nakanishi and T. Shigematsu, Martensitic Transformations in Zirconia Ceramics, *Mater. Trans.*, 1992, **33**(3), p 318-323
  8. X.Q. Cao, R. Vassen, and D. Stöver, Ceramic Materials for Thermal Barrier Coatings, *J. Eur. Ceram. Soc.*, 2004, **24**, p 1-10
  9. S.A. Tsipas, Effect of Dopants on the Phase Stability of Zirconia-Based Plasma Sprayed Thermal Barrier Coatings, *J. Eur. Ceram. Soc.*, 2010, **30**, p 61-72
  10. X.Q. Cao, R. Vassen, W. Jungen, S. Schwartz, F. Tietz, and D. Stöver, Thermal Stability of Lanthanum Zirconate Plasma-Sprayed Coating, *J. Am. Ceram. Soc.*, 2001, **84**(9), p 2086-2090
  11. T. Liu, X.T. Luo, X. Chen, G.J. Yang, C.X. Li, and C.J. Li, Morphology and Size Evolution of Interlamellar Two-dimensional Pores in Plasma-Sprayed  $\text{La}_2\text{Zr}_2\text{O}_7$  Coatings During Thermal Exposure at 1300 °C, *J. Therm. Spray Technol.*, 2015, **24**(5), p 739-748
  12. R. Vassen, M.O. Jarligo, T. Steinke, D.E. Mack, and D. Stöver, Overview on Advanced Thermal Barrier Coatings, *Surf. Coat. Technol.*, 2010, **205**(4), p 938-942
  13. L.L. Cai, W. Ma, B. Ma, F. Guo, W.D. Chen, H.Y. Dong, and Y.C. Shuang, Air Plasma-Sprayed  $\text{La}_2\text{Zr}_2\text{O}_7$ - $\text{SrZrO}_3$  Composite Thermal Barrier Coating Subjected to  $\text{CaO-MgO-Al}_2\text{O}_3\text{-SiO}_2$  (CMAS), *J. Therm. Spray Technol.*, 2017, **26**(6), p 1076-1083
  14. Y. Li, C.J. Li, G.J. Yang, and C.X. Li, Relation Between Microstructure and Thermal Conductivity of Plasma-Sprayed 8YSZ Coating, *Int. J. Mod. Phys. B*, 2010, **24**, p 3017-3022
  15. Q.B. Fan, F. Zhang, F.C. Wang, and L. Wang, Molecular Dynamics Calculation of Thermal Expansion Coefficient of a Series of Rare-Earth Zirconates, *Comput. Mater. Sci.*, 2009, **46**, p 716-719
  16. A. Sharma, T. Dudykevych, D. Sansom, and R. Subramanian, Increased Reliability of Gas Turbine Components by Robust Coatings Manufacturing, *J. Therm. Spray Technol.*, 2017, **26**(6), p 1084-1094
  17. H.X. Wu, Z. Ma, L. Liu, Y.B. Liu, and D.Y. Wang, Thermal Cycling Behavior and Bonding Strength of Single-Ceramic-Layer  $\text{Sm}_2\text{Zr}_2\text{O}_7$ , and Double-Ceramic-Layer  $\text{Sm}_2\text{Zr}_2\text{O}_7$ /8YSZ Thermal Barrier Coatings Deposited by Atmospheric Plasma Spraying, *Ceram. Int.*, 2016, **42**(11), p 12922-12927
  18. P. Carpio, R. Moreno, A. Gómez, M.D. Salvador, and E. Sánchez, Role of Suspension Preparation in the Spray Drying Process to Obtain Nano/Submicrostructured YSZ Powders for Atmospheric Plasma Spraying, *J. Eur. Ceram. Soc.*, 2015, **35**(1), p 237-247
  19. A.H. Pakseresht, M.R. Rahimpour, M.R. Vaezi, and M. Salehi, Thermal Plasma Spheroidization and Spray Deposition of Barium Titanate Powder and Characterization of the Plasma Sprayable Powder, *Mater. Chem. Phys.*, 2016, **173**, p 395-403
  20. P. Fauchais, Topical Review: Understanding Plasma Spraying, *J. Appl. Phys.*, 2004, **37**(9), p 86-108
  21. L.L. Shaw, D. Goberman, R. Ren, M. Gell, S. Jiang, Y. Wang, T.D. Xiao, and P.R. Strutt, The Dependency of Microstructure and Properties of Nanostructured Coatings on Plasma Spray Conditions, *Surf. Coat. Technol.*, 2000, **130**(1), p 1-8
  22. D.R. Clarke, Materials Selection Guidelines for Low Thermal Conductivity Thermal Barrier Coatings, *Surf. Coat. Technol.*, 2003, **163-164**(02), p 67-74
  23. W.G. Chi, S. Sampath, and H. Wang, Microstructure-Thermal Conductivity Relationships for Plasma-Sprayed Yttria-Stabilized Zirconia Coatings, *J. Am. Ceram. Soc.*, 2008, **91**, p 2636-2645
  24. J.A. Thompson and T.W. Clyne, The Effect of Heat Treatment on the Stiffness of Zirconia Top Coats in Plasma-Sprayed TBCs, *Acta Mater.*, 2001, **49**, p 1565-1575
  25. R.S. Lima, S.E. Kruger, G. Lamouche, and B.R. Marple, Elastic Modulus Measurements via Laser-Ultrasonic and Knoop Indentation Techniques in Thermally Sprayed Coatings, *J. Therm. Spray Technol.*, 2005, **14**, p 52-60
  26. S. Guo and Y. Kagawa, Young's Moduli of Zirconia Top-Coat and Thermally Grown Oxide in a Plasma-Sprayed Thermal Barrier Coating System, *Scripta Mater.*, 2004, **50**, p 1401-1406
  27. Y. Tan, A. Shyam, W.B. Choi, E. Lara-Curzio, and S. Sampath, Anisotropic Elastic Properties of Thermal Spray Coatings Determined via Resonant Ultrasound Spectroscopy, *Acta Mater.*, 2010, **58**, p 5305-5315